

Incongruent Melting and Phase Diagram of SiC from Machine Learning Molecular Dynamics

Yu Xie^{*,1}, Senja Ramakers^{2,3}, Menghang Wang¹, Frans Spaepen¹, and Boris Kozinsky^{†,1,4}

¹Harvard John A. Paulson School of Engineering and Applied Sciences

²Ruhr-Universität Bochum

³Robert Bosch GmbH

⁴Robert Bosch LLC

Abstract

Silicon carbide (SiC) is an important technological material, but its high-temperature phase diagram has remained unclear due to conflicting experimental results about congruent versus incongruent melting. Here, we employ large-scale machine learning molecular dynamics (MLMD) simulations to gain insights into SiC decomposition and phase transitions. Our approach relies on a Bayesian active learning workflow to efficiently train an accurate machine learning force field on density functional theory data. Our large-scale simulations provide direct evidence of the incongruent melting of SiC, confirming its decomposition into silicon-rich and carbon phases at high temperature and pressure. During cooling at high pressures, carbon nanoclusters nucleate and grow within the homogeneous molten liquid. During heating, the decomposed mixture reversibly transitions back into a homogeneous SiC liquid. The full pressure-temperature phase diagram of SiC is systematically constructed using MLMD simulations, providing new understanding of the nature of phases, resolving long-standing inconsistencies from previous experiments and yielding technologically relevant implications for processing and deposition of this material.

*yuxie1@microsoft.com. Yu Xie conducted this work at Harvard before joining Microsoft.

†bkoz@seas.harvard.edu

1 Introduction

Silicon carbide (SiC) is an important technological material valued for its high hardness, mechanical strength, high thermal conductivity, and wide band gap [1]. The high-temperature and high-pressure behavior of SiC is of great scientific interest for understanding planetary interiors and stellar processes, due to its identification from adsorption spectroscopy of carbon-rich extrasolar planets [2, 3]. Understanding the properties of SiC under extreme conditions is also crucial for various applications, including nuclear reactors [4], epitaxial deposition growth of SiC [5, 6], and graphene synthesis [7] for electronics and quantum devices.

The melting and decomposition of SiC have been investigated by experimental and computational methods for decades. However, various experiments have reached inconsistent conclusions and thereby raised confusion about the nature of melting of SiC. Experiments at high temperatures and pressures are challenging because it is difficult to directly observe the kinetics of melting, and factors such as sample size and purity, and thermal gradients causing temperature inhomogeneity can further complicate interpretations. In some studies, incongruent melting has been reported, with the observation that SiC decomposes into a silicon rich liquid and solid carbon upon heating [8, 9, 10, 11]. Most of these experiments are performed at pressures below 10 GPa, except for a more recent study with a laser-heated diamond-anvil cell that reaches up to 81 GPa and 3200 K [10]. However, other experimental studies report that SiC melts congruently, without decomposition into different phases [12, 13].

Molecular dynamics (MD) simulations using density functional theory (*ab initio* MD, or AIMD) and various empirical potentials were employed to investigate the melting process of SiC with computational simulations. Phase separation and decomposition were not observed, possibly due to the limitation of the small supercell in AIMD [14, 15]. The AIMD results showed some carbon aggregations within amorphous SiC, resulting in a carbon-carbon (C-C) peak at a graphite / diamond bond length of 1.5 Å in their radial distribution functions (RDF). However, these simulations mainly reveal a dominance of Si-C bonds in the system, with only a minor presence of nanoclusters, and do not capture any decomposition according to the RDF. On the other hand, empirical potentials,

such as the Vashishta potential [16], the Tersoff potential [17, 18, 19], and the Gao-Weber potential [20], provide differing descriptions of uncertain accuracy. For example, simulations using the Vashishta potential show no formation of C-C bonds in either liquid or amorphous SiC. Similar to AIMD, the Tersoff potentials [17, 18], the Gao-Weber potential [20], and a recent Behler-Parrinello neural network potential [21] studied the melting of SiC at high temperature and low to moderate pressure (0-10 GPa), showing RDF characteristics where Si-C bonds dominate, with minor C-C bonds signatures. Therefore, the decomposition and phase separation in the amorphous phase of SiC and its melting process remain underexplored and inconsistent across *ab initio*, empirical, and machine learning atomistic simulations, as well as experimental observations.

To overcome the limitations of previous studies, we employ a machine learning force field (MLFF) trained on density functional theory (DFT) data. First, we collect DFT data for different SiC phases and train an MLFF to describe atomic interactions using a hierarchical Bayesian active learning workflow. This approach efficiently explores the phase space across different temperatures, pressures, and compositions. Then, we perform large-scale molecular dynamics simulations, enabled by GPU acceleration, to reliably model the melting and decomposition of SiC at a sufficient scale. By conducting two-phase coexistence simulations, where the interface between two phases of interest is created and equilibrated, we quantitatively determine, for the first time, the transition temperatures between phases at different pressures.

Our simulations conclusively demonstrate the occurrence of incongruent melting at high pressure and the decomposition of SiC into Si and C phases. The transition temperatures between the zinc-blende SiC, decomposed incongruent mixture, and the homogeneous liquid phase are identified by our simulations, at pressures ranging from 30 GPa to 120 GPa. We obtain the pressure-temperature phase diagram depicting the stability regions of different phases. Notably, our findings of the decomposition indicate that amorphous SiC can only be produced through irradiation, not via melt-quench processes, consistent with existing experimental approaches [22, 23]. Our atomic-level results provide microscopic insights into the decomposition and melting behavior

of this technologically important material, resolving discrepancies in previous experimental and computational studies.

2 Methods

Machine learning force field and Bayesian active learning. Accurately modeling the melting and decomposition of SiC at high temperature and pressure requires an interatomic potential that captures complex bonding environments, including phase separation. Traditional empirical force fields, such as Tersoff [18] or Vashishta [16] potentials, often fail to accurately describe bond breaking and phase transitions. While AIMD [14, 15] provides accurate atomic forces, its high computational cost limits simulations to small system sizes and short timescales. To overcome these challenges, we employ a MLFF trained on DFT calculations, such that the atomic interactions can be modeled with high accuracy, while remaining cost effective for large-scale simulations.

Our MLFF is built using the FLARE framework [24, 25], which is based on a sparse Gaussian process model [26] with atomic cluster expansion descriptors [27]. This model predicts forces while providing uncertainty quantification. To efficiently generate training data, we employ Bayesian active learning, which systematically selects new atomic configurations where the MLFF is most uncertain. The workflow follows these steps: (1) Initial Training: The MLFF is first trained on a small set of DFT-calculated structures, including perfect and slightly perturbed crystal structures. (2) Uncertainty-Guided MD: The MLFF runs MD simulations, predicting atomic forces while simultaneously estimating its uncertainty. (3) Selective DFT Calculations: If the model’s uncertainty exceeds a threshold, new configurations are labeled using DFT. Otherwise, continue with MD. (4) Iterative Refinement: The MLFF is retrained with the newly acquired DFT data, progressively improving its accuracy. This adaptive learning process ensures that the force field is only trained where necessary, avoiding redundant DFT calculations while capturing the relevant phase space. Once the active learning is complete, we map the SGP into an equivalent but more computationally efficient polynomial model [25, 26], which serves as the final MLFF for large-scale production simulations in LAMMPS [28]. The DFT calculations are performed using VASP [29] with the PBE

exchange correlation functional [30], following the computational settings in our previous works [25, 31].

The training set is initialized with structures from our previous study [25], encompassing the hexagonal 2H/4H/6H polytypes, B3 (zinc blende or 3C) and the high pressure B1 (rock salt) phases. We then employ the FLARE Bayesian active learning workflow to systematically sample data that captures melting and decomposition behavior across different pressures. Active learning simulations are performed at 0, 30, 60, 90, and 120 GPa over a temperature range of 2000-6000 K until melting is observed. Additional data is collected for pure carbon (diamond and graphite phases, 2000-4000 K) and pure silicon (1000-3000 K) across all pressure conditions. The trained MLFF is then used to investigate SiC melting and decomposition under high temperature and pressure conditions.

Large-scale molecular dynamics simulation. The large-scale molecular dynamics simulations are conducted using GPU-accelerated LAMMPS with Kokkos parallelization [32] and the FLARE MLFF pairstyle, which has demonstrated exceptional performance in billion-atom catalytic simulations [33]. During the melting simulations, the NPT ensemble with anisotropic (*aniso*) control of cell dimensions is employed, allowing independent scaling along the x , y and z directions through stress components P_{xx} , P_{yy} , and P_{zz} . Phase separation exhibits a tendency to minimize the interface between decomposed phases, necessitating anisotropic elongation of the supercell, as illustrated in Fig.1 and Fig.2.

3 Results

3.1 Higher-temperature liquid decomposition and phase separation

As described in the Method section, the MLFF was iteratively refined via Bayesian active learning to ensure accuracy across the phase space, while allowing us to simulate large systems efficiently. We performed Bayesian active learning hierarchically [34], starting with a 64-atom supercell, and then extends to a 512-atom supercell. The 64 atom cell is insufficient for capturing the decomposition, while the larger 512-atom supercell enables observation of the phase separation process. As shown in Fig.1, the phase decomposition occurs at the pressure of 30 GPa during the active learning

process, prior to which the carbon and silicon atoms form clusters instead of mixing homogeneously. As a result, the active learning simulation collects DFT data from both Si-rich and C-rich regimes. This observation also provides evidence for the existence of incongruent melting and decomposition even in small-scale simulations. Nevertheless, to avoid finite size effects, much larger simulations are necessary to quantify the phase transition temperature.

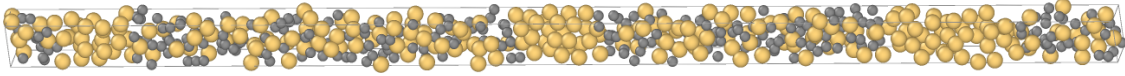


Figure 1: DFT data collected during active learning simulation with 512 atoms at $P = 30$ GPa, $T = 5000$ K.

Starting with the well-trained MLFF model, we run large-scale heating and cooling simulations at 30, 60, and 80 GPa to investigate the phase transformation and decomposition of SiC. We start with a 512,000-atom bulk crystal supercell of the cubic zinc-blende (ZB/3C/B3) phase. At these pressures, decomposition does not occur readily during the MD simulations due to hysteresis, even when heating the cubic ZB crystal structure to temperatures as high as 4000 K. The crystal structure is only destroyed when the temperature is increased to 5000 K.

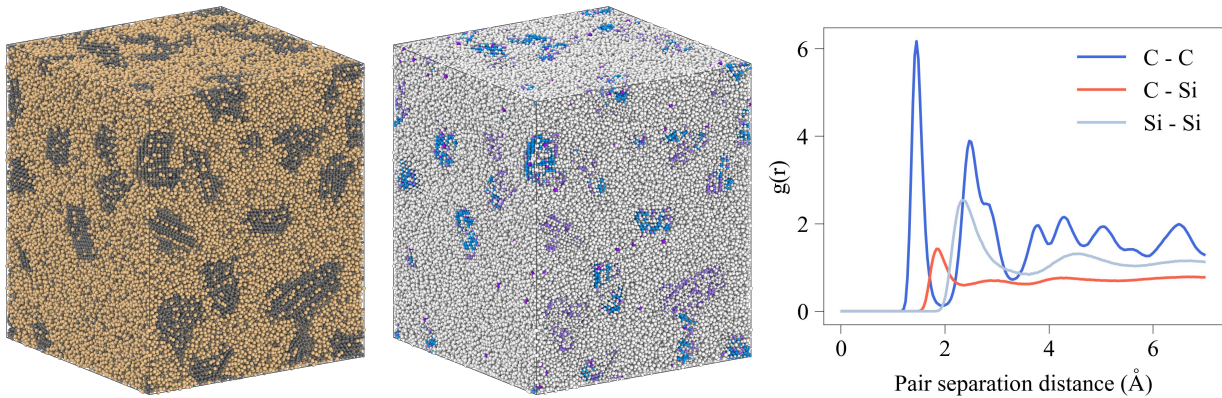


Figure 2: Left: decomposed configuration of 512,000 atoms at the end of the simulation at 3000 K and 60 GPa. Yellow: Si, black: C. Middle: atoms colored with lattice type classified by polyhedral template matching. Blue: cubic diamond, orange: hexagonal diamond, purple: graphite, white: others. Right: radial distribution function of the structure.

At ambient pressure (close to 0 GPa), we observe sublimation as the unit cell volume expands, causing the SiC crystal to break into small molecules, consistent with experimental observations. In contrast, at pressures of 30, 60, and 80 GPa, sublimation is not observed.

At 5000 K, small separate carbon and silicon clusters form in the amorphous configurations, which indicates a trend away from a homogeneous mixture of silicon and carbon. Even though the temperature is significantly higher than experimentally reported incongruent or congruent melting points [8, 9, 10, 11, 35], the complete phase separation of C and Si does not occur. Upon cooling the system to 3000 K, we observe decomposition into carbon crystals and silicon liquid. Specifically, as the temperature drops below 4000 K, carbon clusters start to grow in size, while the Si concentration in the liquid phase increases. Upon further cooling to 3000 K, larger C clusters consisting of recognizable graphite or diamond crystal structure form within the Si-rich liquid.

The formation of either graphite or diamond C phases depends on the simulation pressure. The C clusters are classified as graphite-like or diamond-like structures by the polyhedral template matching [36] implemented in OVITO [37]. At 30 GPa, C clusters form graphite-like honeycomb lattice structures, while the Si-rich liquid persists throughout our simulation temperature range (3000-5000 K), which is higher than the Si melting point (1684 K at 0 GPa [38]). At 60 GPa, the diamond and graphite-like clusters incorporate Si atoms within them, as illustrated in Fig.2. In addition, the C-C pair distribution function exhibits a dominant peak around 1.5 Å, while the C-Si peak decreases. At 80 GPa, the decomposition results in the separation of diamond C, liquid Si, and the high-pressure rock-salt (RS/B1) phase of SiC. The configurations at 30 GPa and 80 GPa are shown in the Supplementary Materials. Our results agree with a recent experimental observation [10] that solid C and liquid Si form upon melting (i.e., incongruent melting) of SiC at high pressures. At 120 GPa, the zinc blende to rock salt phase transition occurs, and the high pressure stabilizes the crystal structure and prevents it from amorphization, with no liquid phase appearing up to 5000 K.

3.2 High temperature transition from decomposed Si + C to homogeneous liquid

Having established that decomposition occurs, we next explore the phase transition between the decomposed and homogeneous liquid states. To verify the reversibility of the incongruent high-pressure melting and to quantitatively identify the transition temperature and pressure of the spontaneous decomposition, we set up a smaller MD simulation with slower cooling and heating rates.

Specifically, we start with 8,000 atoms in the zinc-blende (B3) phase of SiC at 5000 K, so that the crystal becomes a homogeneous liquid. With a time step of 0.5 fs, we perform an equilibration for 0.5 ns at each temperature, followed by a 0.5 ns cooling process at a rate of 400 K/ns. We alternate between equilibration and cooling steps until reaching 3000 K, then we ramp the temperature back up to 5000 K following the same scheme. The temperature profile over simulation time is shown as the blue curve in the lower panel of Fig.3.

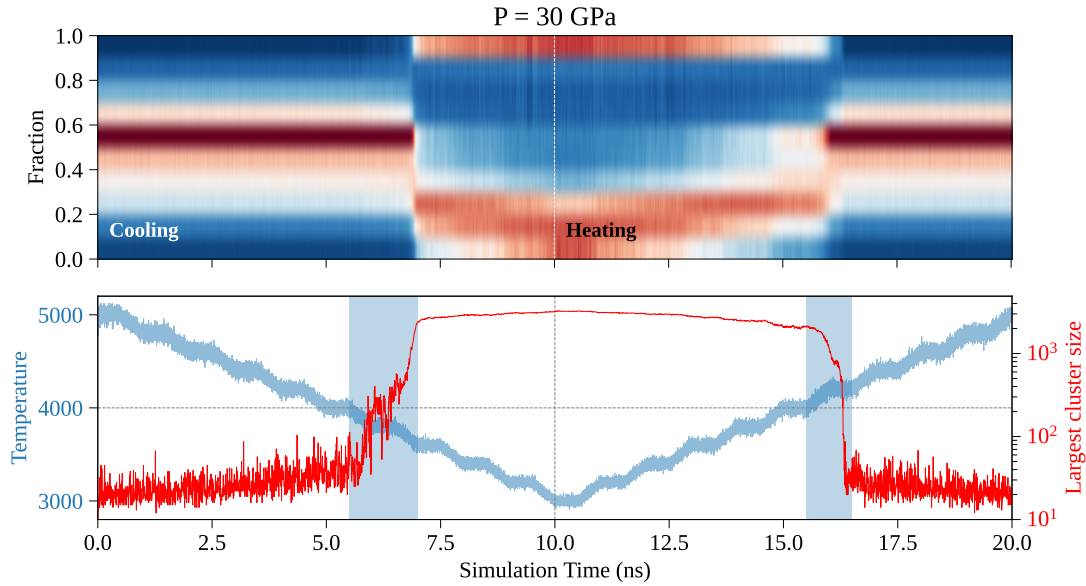


Figure 3: Cooling and heating simulation of SiC at 30 GPa, illustrating the transition between decomposed Si + C and homogeneous liquid. Top: population distribution of local C atom fraction with the simulation time. Red: high population, blue: low population. Bottom: temperature (blue) and largest carbon cluster size (red) (number of atoms) with the simulation time. Blue shadows indicate the phase transition regions.

To quantitatively identify spontaneous phase separation, we use the local C fraction (concentration) as the order parameter and track the size of the largest C cluster. At each time step, we divide the simulation cell into $10 \times 10 \times 10$ voxels and calculate the C atom fraction in each voxel. The population of voxels with different local fraction levels over time is represented by the color scale in the top panel of Fig.3, with red indicating higher populations.

At the beginning of the simulation, at a pressure under 30 GPa and a high temperature of 5000 K, we observe a high population of 0.5 local C fraction values, indicating a homogeneous liquid with

equal mixture of Si and C atoms. The lower panel of Fig.3 shows the system temperature and the largest C cluster size. As the system cools, the largest C cluster size increases, notably around 4000 K. At 7 ns, when the system cools down to 3600 K, spontaneous decomposition is finished, with C atoms mostly depleted from the Si liquid. The local C-fractions are either near 0 (Si rich) or near 1 (C rich), as indicated in the upper panel.

During heating, the reverse process initiates at the same transition temperature of approximately 4000 K. The C cluster dissolves into the Si liquid, and the local C fraction returns to around 0.5, analogous to the initial state of the simulation. This indicates that the system has returned to the homogeneous liquid upon heating. Similar results are obtained for 60 GPa and 90 GPa, which are shown in the Supplementary Materials.

3.3 Lower temperature transition from crystalline to decomposed Si + C

Having identified the high-temperature transition between the incongruently decomposed Si + C mixture and the homogeneous liquid phase, we investigate the lower-temperature transition between the crystal B1 or B3 phases and the decomposed phase. To overcome hysteresis and high nucleation barriers that prevent decomposition in direct MD simulations of B3 SiC crystals heated to 4000 K, we employ two-phase coexistence simulations. This approach, comprising four stages [39, 40], allows us to quantitatively determine the transition temperatures: 1) Equilibrate the crystalline supercell at pressure P (30, 60, 90 GPa) and an initially estimated transition temperature T_{es} . 2) Fix the positions and velocities of half the atoms in a slab along z-axis and heat the other half up to T_h (much higher than T_{es}) in the $NP_{zz}T$ ensemble to induce a transition to the liquid phase. 3) Cool the heated region from T_h to T_{es} in the $NP_{zz}T$ ensemble, forming the decomposed phase while maintaining the unheated crystalline half. 4) Remove constraints on the crystalline region and equilibrate the entire system in the NPH ensemble, allowing the phase boundary to move. In stages 1-3, we create an interface between the crystalline and decomposed phases. In the last stage, the system equilibrates near the transition temperature. If both phases coexist at equilibrium, we identify this temperature as the phase transition temperature.

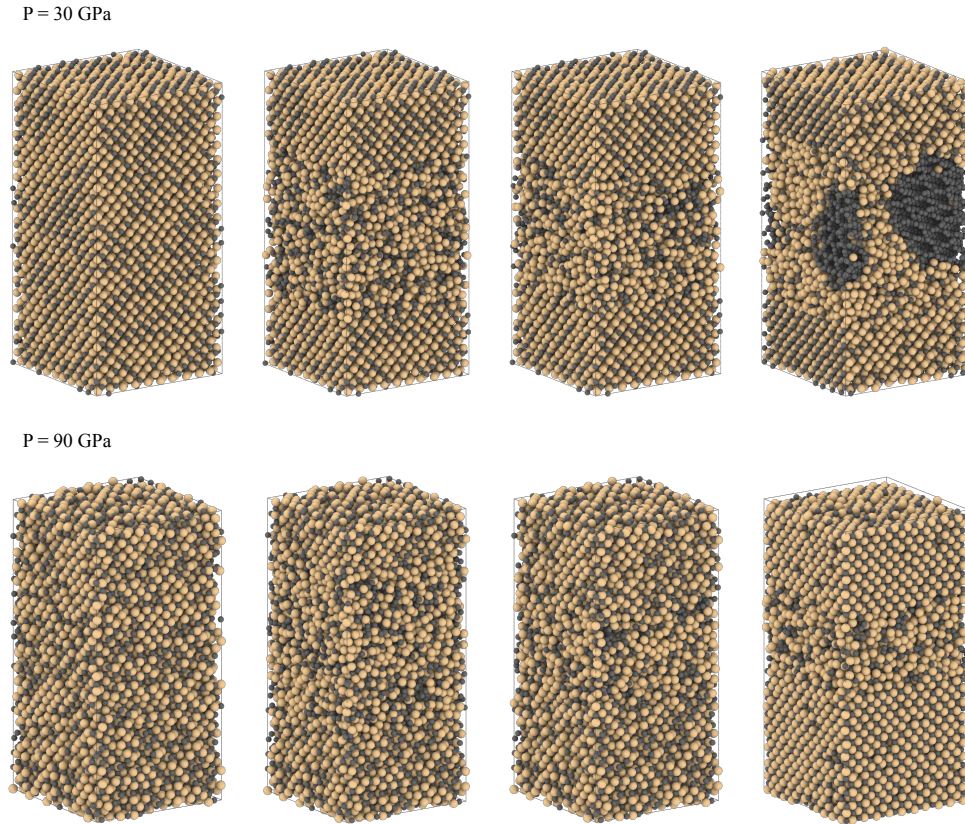


Figure 4: Snapshots of the four stages of the two-phase MD at 30 GPa (top) and 90 GPa (bottom) pressures. Each stage is simulated for 0.5 ns.

Each of the four stages is simulated for 0.5 ns, and the snapshots at the end of each stage are shown in Fig. 4 for the pressure values of 30 GPa (starting with B3 zinc blende) and 90 GPa (starting with B1 rock salt). In the last stage of the two-phase simulation where the interface is allowed to move, the temperature of the entire system fluctuates and converges to the actual transition temperature at which the decomposed and crystalline phases coexist in equilibrium, and the interface stops moving.

Fig.5 shows the results of the heating and cooling process in the two-phase coexistence simulations for different initial temperatures near the expected transition temperature.

At the fixed pressure of 30 GPa, during the heating stage (0.5-1 ns), the heated half of the supercell becomes amorphous, and the overall fraction of zinc-blende local structures in the supercell decreases to 0.5. The C clusters begin to form during the cooling stage (1-1.5 ns) and continue growing in size at 1.5-2 ns as demonstrated in the second column of Fig.5. In the NPH simulation

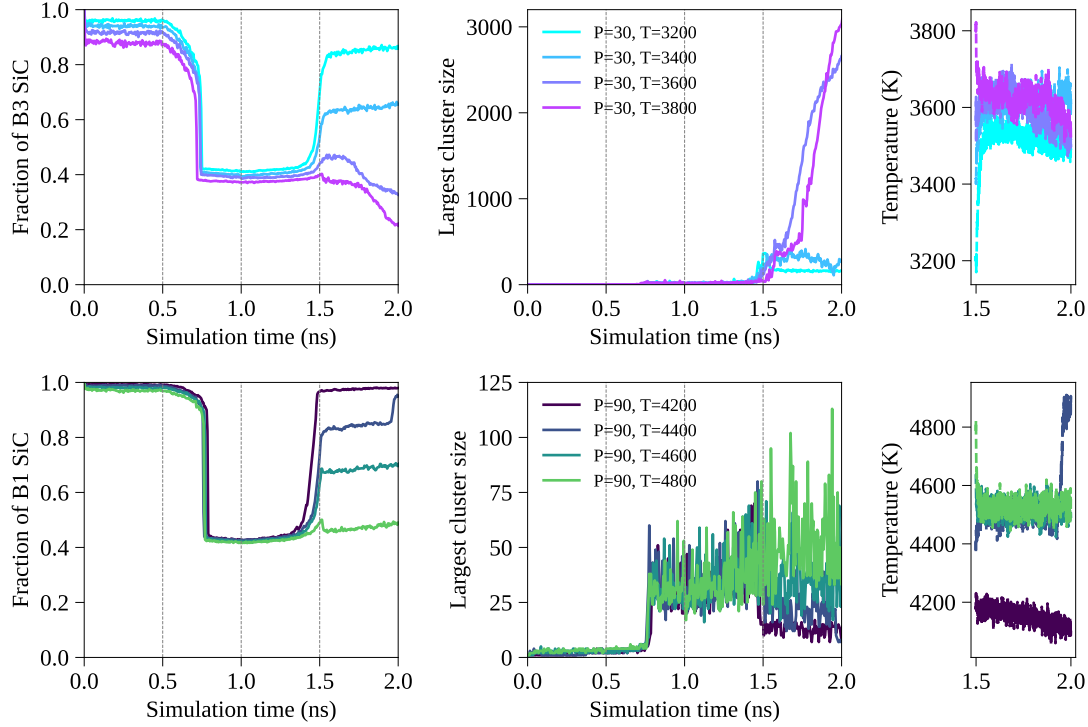


Figure 5: Analysis of two-phase coexistence simulations. Panels (left to right) show: fraction of zinc-blende (rock-salt) structures, largest C cluster size (number of atoms), temperature convergence at the NPH stage, over simulation time. Top: 30 GPa. Bottom: 90 GPa.

stage (1.5-2 ns), both B3 crystal and decomposed Si + C phases coexist, with relatively different equilibrated fractions dependent on the initial temperature. Meanwhile, multiple simulations with different initial temperatures converge to approximately 3500 K during the NPH stage, which is identified as the transition temperature (shown in the third column of Fig.5).

At 90 GPa, where the stable phase at low temperature is rock salt (B1), a similar procedure starting from B1 phase yields a transition temperature around 4500 K. Notably, the carbon cluster sizes formed at 90 GPa are much smaller than those at 30 GPa, leading us to conjecture that at sufficiently high pressures, the decomposed Si+C phase between the crystalline and liquid phases may not be present. Additional coexistence simulations were performed at 10 GPa and 60 GPa, with results presented in the Supplementary Materials.

3.4 Phase diagram

Here we combine the results obtained from the MD simulations of the SiC phase transitions into a complete pressure-temperature phase diagram. Fig.6 presents the P - T diagram, illustrating the $B3 \leftrightarrow B1$, $B3 \leftrightarrow \text{gas}$, $B3 \leftrightarrow \text{Si} + \text{C}$, $B1 \leftrightarrow \text{Si} + \text{C}$, and $\text{Si} + \text{C} \leftrightarrow \text{SiC}$ (liquid) transitions. For completeness, we briefly describe the simulations of $B3 \leftrightarrow B1$ transition and $B3 \leftrightarrow \text{gas}$ below, although these are not the primary focus of this work.

The $B3 \leftrightarrow B1$ transition pressures at various temperatures are determined using the same methods as in our previous work [25]. Starting with the B3 crystal, we increase pressure at a fixed temperature to generate a configuration containing both phases. Then, we perform constant-pressure MD simulations on these coexistence structures at different pressures to identify the transition point, characterized by the stable coexistence of two phases remains. The pressure scan results are shown in the Supplementary Materials. The $B3 \leftrightarrow B1$ transition pressures identified from our simulations (black solid line in Fig. 6) are close to experimental measurements with a deviation of less than 20 GPa.

At zero or low pressure, the SiC B3 crystal sublimates into gas phase instead of melting, which only occurs under high pressure. Our MD simulation at $T = 4000$ K and $P = 0$ -10 GPa show a continuous increase in cell volume (Supplementary Figure 9), indicating that the bulk crystal tends to sublime into small molecules and single atoms. This evaporation is expected at low pressures and high temperatures. In our two-phase coexistence simulation at a low pressure of 10 GPa, the decomposed phase presents significant deformation and stress, further indicating instability of the bulk structure under these conditions.

The transition temperatures that we observe between B3 and decomposed Si + C at high pressures are significantly higher than those reported in a previous experiment by Daviau et al. (blue-orange circles) [10]. This discrepancy may be attributed to the challenges in high-pressure measurements and the likely presence of significant temperature gradients and transients in the diamond anvil setup (see more details in the *Discussions* section). Nevertheless, at pressures around 10 GPa,

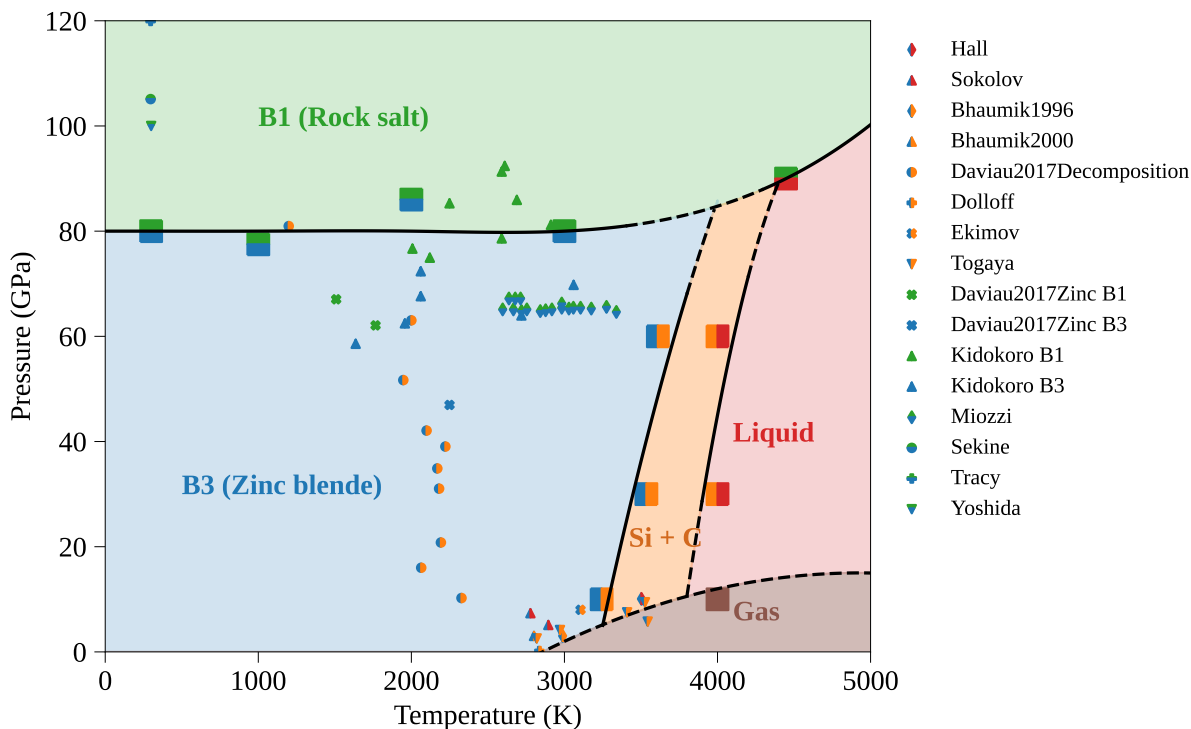


Figure 6: Phase diagram of SiC. Results from our MD simulations are denoted in big squares, and the inferred phase boundaries are drawn with black solid lines (interpolated) and dash lines (extrapolated). Blue: B3 (ZB), green: B1 (RS), orange: decomposed Si + C, red: homogeneous liquid, brown: gas. The background colors indicate the stability regions of different phases inferred by our simulations. Experimental reports of congruent melting (blue-red): diamond [12], triangle [13]. Incongruent melting (blue-orange): diamond [11], triangle [35], circle [10], plus [41], cross [8], upside-down triangle [9]. B3-B1 transition (blue-green): cross [42], triangle [43], diamond [44], circle [45], plus [46], upside-down triangle [47].

our transition temperature is consistent with experimental results by Togaya et al. (blue-orange upside-down triangles) [9].

The high-temperature phase boundary is close to the melting point of graphite and diamond carbon, indicating that the C clusters dissolve at around 4000 K and SiC becomes a homogeneous liquid mixture. As depicted in Supplementary Figure 1, the Si-C peak indicates that the Si and C are mixed well, and the complete phase separation does not occur, as opposed to the RDF shown in Fig. 2.

4 Discussions

Our MLFF, based on Gaussian process regression [26], provides uncertainty estimations for its predictions. To ensure the fidelity of our large-scale MD simulations, we assess whether high-uncertainty configurations are involved. A sufficient training dataset covering a variety of configurations results in low uncertainties during simulations, as the model is familiar with the encountered atomic structures. Conversely, high model uncertainty implies the MD has proceeded to configurations not covered by the training data, potentially reducing prediction reliability.

Therefore, we evaluate the model uncertainty on snapshots from the decomposition MD simulations. As shown in Supplementary Figure 11, the model uncertainty remains well below the acquisition criteria of our force field active learning workflow. This indicates that our collected training data set sufficiently covers the configuration space, ensuring high confidence level in the model predictions.

In our MD simulation where decomposition occurs, we cannot directly model the transition from a pure crystal B3 phase to the decomposed phase due to hysteresis and nucleation barriers. Instead, we must overheat and amorphize the crystal SiC to a homogeneous liquid before decomposition can take place during the cooling stage. Meanwhile, experimental observations align with this approach, demonstrating that the decomposition originates from the heating and cooling processes. For example, Daviau and Lee reported no evidence of decomposition in the Raman spectra when heating to 3200 K at 81 GPa. However, the surrounding region, annealed to 1200 K, showed D and G band signatures of carbide-derived carbon [10]. Similarly, Togaya and Sugiyama [9] reported using a sample quenched from a molten state to determine the onset of fusion, further supporting the importance of cooling in the decomposition process.

While numerous experiments have confirmed the occurrence of incongruent melting or decomposition in SiC, some studies have reported congruent melting. Considering the slow kinetics of SiC decomposition and phase transformation, the grain size can influence the process. For instance, in experiments reporting congruent melting, large single crystalline grains (between 150 μm and 3 mm) are used, which likely hinders the transition [13].

While our MD simulations confirm incongruent melting at various pressures, qualitatively consistent with the experiment [10], our obtained transition temperatures at high pressures are significantly higher than the reported measurements around 2000 K. This discrepancy may be attributed to several factors in experimental setups: (1) Since the temperature is measured via the thermal emission from the surface, the approach could underestimate the core temperature. (2) The heat distribution in the sample could be inhomogeneous, such that overheating in certain regions might facilitate the decomposition at lower apparent temperatures. Although there are no other experimental reports at such high pressures, our simulation is in good agreement with the transition temperature at a lower pressure of 10 GPa found in another experiment [9]. We also note that in other applications, such as physical deposition vapor growth of SiC, a temperature of ~ 2500 K is used at ~ 0 GPa, demonstrating SiC's stability at temperatures higher than 2000 K [48]. This observation further supports the plausibility of our higher predicted transition temperatures at elevated pressures.

The two-phase coexistence MD simulation creates an interface between two different phases and thereby overcomes the nucleation barrier. It is possible that the defect concentration influences the phase transition temperature. Even state of the art epitaxially grown SiC wafers have high defect densities [48], implying that non-optimized powered SiC contains large amounts of defects. Therefore, we performed additional simulations, in which we introduce different point defect concentrations in the crystal. As shown in Supplementary Figure 7, the concentration of defects does not have a significant influence on the transition temperature converged by the two-phase MD simulation. Macroscopic defects such as dislocations and phase boundaries could have a greater impact than point defects but are out of scope of this study.

While some previous computational studies using empirical and neural network potentials obtain amorphous SiC through melting and quenching [20, 21], our simulations show that the melting and quenching process results in the decomposition of the SiC. Instead, techniques such as irradiation are required for the amorphization of SiC, which is consistent with most of the experiments [22, 23]. Building upon our findings on SiC decomposition, we now explore possible mechanisms underlying this process. The two primary mechanisms to consider are nucleation and spinodal decomposition.

To investigate spinodal decomposition, we calculated the C-C spatial correlation function from local concentrations (Supplementary Figure 10). Notably, towards the end of cooling process, particularly below 3400 K, a peak appears at approximately 40 Å. This implies periodic fluctuations in the carbon concentration, indicative of a wavelength of the phase separation mode [49, 50]. This observation aligns with the spinodal decomposition mechanism reported in alloy systems [49, 50] and is consistent with a recent tight-binding MD study of SiC under tensile stresses [51]. To analyze the nucleation of solid carbon clusters during decomposition, we tracked the evolution of diamond and graphite clusters. Fig.7 illustrates the various stages of carbon cluster development, highlighting their transformation into either diamond or graphite phases. We applied cluster analysis in OVITO [37] with a 1.55 Å cutoff - approximately the bond length in graphite and diamond - to identify clusters. The formation of different phases were analyzed by the "identify diamond structure" method [52] for diamond, and polyhedral template matching [36] for graphite. We track the evolution of clusters by identifying those with the largest overlap with the final structures at each time step. As shown in Fig.7, in earlier stages, small nuclei lack clear lattice symmetry or phase identity. For graphite, the hexagonal structure can be traced back to smaller clusters. However, tracking becomes challenging for clusters below 100 atoms, as dynamic rearrangements reduce the overlap ratio quickly over time for both diamond and graphite structures.

In conclusion, our machine learning molecular dynamics study confirms the occurrence of incongruent melting in SiC, with the decomposition of SiC into Si and C being observed at a temperature range of 3200 - 3600 K at high pressures. We also identified a transition at higher temperatures where the decomposed phase transforms into a homogeneous liquid phase. The highly efficient and accurate MLFF enabled previously intractable modeling and simulation of the decomposition process, overcoming limitations of both *ab initio* or empirical force fields in terms of computational cost and accuracy. Our MD simulations provide atomic-level insights, revealing nucleation mechanisms and process details inaccessible in experiments. These findings support the existence of incongruent melting at high pressure, clarifying controversial experimental observations. In summary, our study provides a comprehensive understanding of SiC melting and decomposition

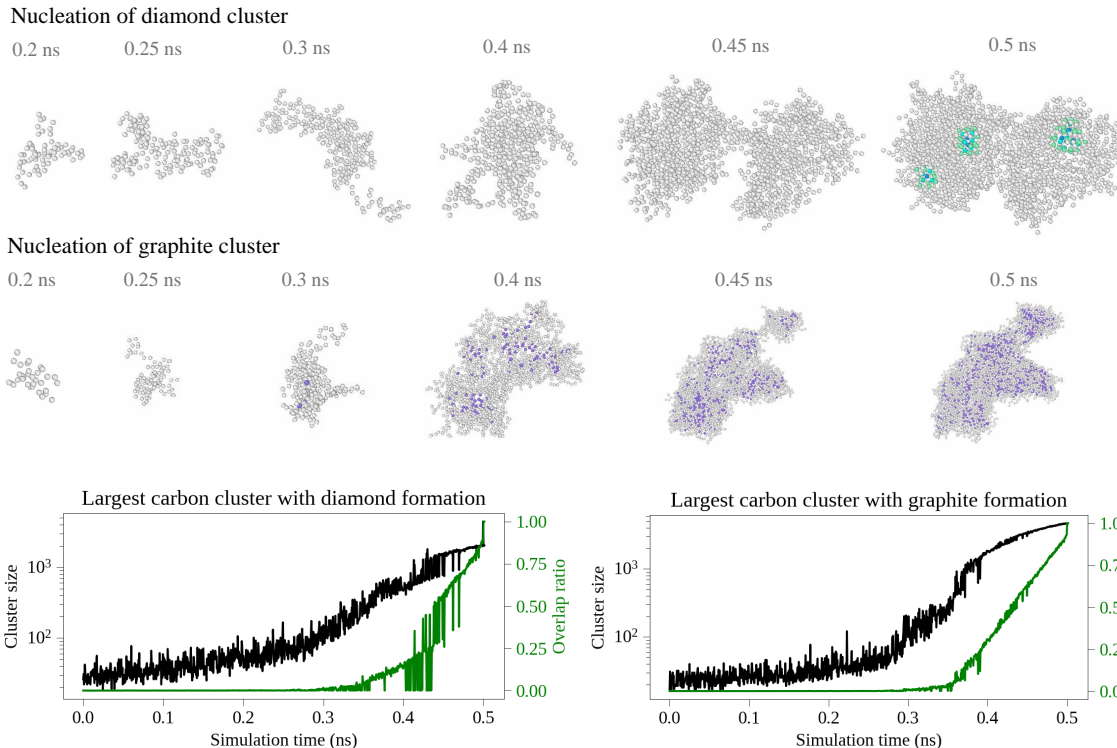


Figure 7: Nucleation analysis of carbon clusters from simulations of 512,000 atoms. Top: Nucleation of diamond cluster at 60 GPa. Diamond core is colored in cyan. Middle: Nucleation of graphite cluster at 30 GPa. Graphite core is colored in purple. Bottom: Increase of the diamond cluster (left) and graphite cluster (right) size and its overlap with the final largest cluster, with simulation time.

behavior, along with a complete phase diagram, reconciling and extending previous experimental and theoretical work in this field.

5 Data Availability

The data and scripts are available on Zenodo <https://doi.org/10.5281/zenodo.14648292>.

6 Acknowledgement

We acknowledge Cameron Owen and Anders Johansson for discussions and help with large simulation setup and computational resources. We acknowledge Evelyn Hu for helpful discussions and feedback. Y.X. is supported by the “Design & Assembly of Atomically-Precise Quantum Materials & Devices” grant DE-SC0020128 of Department of Energy. M.W. is supported by National Science

Foundation, Office of Advanced Cyberinfrastructure (OAC), under Award No. 2118201. B.K. and F.S. are supported by the Harvard University Materials Research Science and Engineering Center funded by the National Science Foundation grant DMR-2011754. The simulation and analysis are done on Harvard Cannon cluster. This research used resources of the National Energy Research Scientific Computing Center (NERSC), a DOE Office of Science User Facility supported by the Office of Science of the U.S. Department of Energy under Contract No. DE-AC02-05CH11231 using NERSC award BES-ERCAP0024206.

7 Author Contributions

Y.X. initiated the project, performed the training of the ML force field, the simulations of the SiC phase transitions and post analysis of the data. S.R. contributed to the DFT settings, and the collection of experimental results. M.W. contributed to the dataset and code preparation. F.S. guided the analysis of nucleation and decomposition. B.K. supervised all aspects of the project. All authors contributed to the writing of the manuscript.

References

- [1] Madar, R. Silicon carbide in contention. *Nature* **430**, 974–975 (2004).
- [2] Madhusudhan, N., Lee, K. K. & Mousis, O. A possible carbon-rich interior in super-earth 55 cancri e. *Astrophys. J. Lett.* **759**, L40 (2012).
- [3] Speck, A., Barlow, M. & Skinner, C. The nature of the silicon carbide in carbon star outflows. *Mon. Notices Royal Astron. Soc.* **288**, 431–456 (1997).
- [4] Katoh, Y. & Snead, L. L. Silicon carbide and its composites for nuclear applications—historical overview. *Journal of Nuclear Materials* **526**, 151849 (2019).
- [5] Matsunami, H. & Kimoto, T. Step-controlled epitaxial growth of sic: High quality homoepitaxy. *Materials Science and Engineering: R: Reports* **20**, 125–166 (1997).
- [6] Yi, J., He, X., Sun, Y. & Li, Y. Electron beam-physical vapor deposition of sic/sio₂ high emissivity thin film. *Applied surface science* **253**, 4361–4366 (2007).

- [7] Zhang, W. & Van Duin, A. C. Atomistic-scale simulations of the graphene growth on a silicon carbide substrate using thermal decomposition and chemical vapor deposition. *Chemistry of Materials* **32**, 8306–8317 (2020).
- [8] Ekimov, E. *et al.* A high-pressure cell for high-temperature experiments in a toroid-type chamber. *Instruments and Experimental Techniques* **47**, 276–278 (2004).
- [9] Togaya, M. & Sugiyama, S. Melting behavior of β -sic at high pressure. *The Review of High Pressure Science and Technology* **7**, 1037–1039 (1998).
- [10] Daviau, K. & Lee, K. K. Decomposition of silicon carbide at high pressures and temperatures. *Phys. Rev. B* **96**, 174102 (2017).
- [11] Bhaumik, S., Divakar, C., Mohan, M. & Singh, A. A modified high-temperature cell (up to 3300 k) for use with a cubic press. *Review of scientific instruments* **67**, 3679–3682 (1996).
- [12] Hall, H. T. High temperature studies. *Bringham Young University: Provo, UT, USA* 36 (1956).
- [13] Sokolov, P. S., Mukhanov, V. A., Chauveau, T. & Solozhenko, V. L. On melting of silicon carbide under pressure. *Journal of Superhard Materials* **34**, 339–341 (2012).
- [14] Finocchi, F., Galli, G., Parrinello, M. & Bertoni, C. M. Microscopic structure of amorphous covalent alloys probed by ab initio molecular dynamics: Sic. *Physical review letters* **68**, 3044 (1992).
- [15] Saiz, F. An ab initio study on liquid silicon carbide. *J Phys. Chem. Solids* **137**, 109204 (2020).
- [16] Vashishta, P., Kalia, R. K., Nakano, A. & Rino, J. P. Interaction potential for silicon carbide: A molecular dynamics study of elastic constants and vibrational density of states for crystalline and amorphous silicon carbide. *J. Appl. Phys.* **101**, 103515 (2007).
- [17] Tersoff, J. Modeling solid-state chemistry: Interatomic potentials for multicomponent systems. *Physical review B* **39**, 5566 (1989).
- [18] Tersoff, J. Chemical order in amorphous silicon carbide. *Physical Review B* **49**, 16349 (1994).

- [19] Yan, W., Gao, T., Guo, X., Qin, Y. & Xie, Q. Melting kinetics of bulk sic using molecular dynamics simulation. *Science China Physics, Mechanics and Astronomy* **56**, 1699–1704 (2013).
- [20] Devanathan, R., Gao, F. & Weber, W. J. Atomistic modeling of amorphous silicon carbide using a bond-order potential. *Nucl. Instrum. Methods Phys. Res. B* **255**, 130–135 (2007).
- [21] Kubo, A. & Umeno, Y. Machine-learning-based atomistic model analysis on high-temperature compressive creep properties of amorphous silicon carbide. *Materials* **14**, 1597 (2021).
- [22] Snead, L., Zinkle, S., Hay, J. & Osborne, M. Amorphization of sic under ion and neutron irradiation. *Nuclear Instruments and Methods in Physics Research Section B: Beam Interactions with Materials and Atoms* **141**, 123–132 (1998).
- [23] Ishimaru, M., Bae, I.-T. & Hirotsu, Y. Electron-beam-induced amorphization in sic. *Physical Review B* **68**, 144102 (2003).
- [24] Vandermause, J. *et al.* On-the-fly active learning of interpretable bayesian force fields for atomistic rare events. *npj Comput. Mater.* **6**, 1–11 (2020).
- [25] Xie, Y. *et al.* Uncertainty-aware molecular dynamics from bayesian active learning for phase transformations and thermal transport in sic. *npj Computational Materials* **9**, 36 (2023).
- [26] Vandermause, J., Xie, Y., Lim, J. S., Owen, C. J. & Kozinsky, B. Active learning of reactive bayesian force fields applied to heterogeneous catalysis dynamics of h/pt. *Nature Communications* **13**, 5183 (2022).
- [27] Drautz, R. Atomic cluster expansion for accurate and transferable interatomic potentials. *Phys. Rev. B* **99** (2019).
- [28] Thompson, A. P. *et al.* LAMMPS-a flexible simulation tool for particle-based materials modeling at the atomic, meso, and continuum scales. *Computer Physics Communications* **271**, 108171 (2022).
- [29] Kresse, G. & Hafner, J. Ab initio molecular dynamics for liquid metals. *Physical review B* **47**, 558 (1993).

- [30] Perdew, J. P., Burke, K. & Ernzerhof, M. Generalized gradient approximation made simple. *Physical review letters* **77**, 3865 (1996).
- [31] Ramakers, S. *et al.* Effects of thermal, elastic, and surface properties on the stability of sic polytypes. *Phys. Rev. B* **106**, 075201 (2022).
- [32] Trott, C. R. *et al.* Kokkos 3: Programming model extensions for the exascale era. *IEEE Transactions on Parallel and Distributed Systems* **33**, 805–817 (2022).
- [33] Johansson, A. *et al.* Micron-scale heterogeneous catalysis with bayesian force fields from first principles and active learning. *arXiv preprint arXiv:2204.12573* (2022).
- [34] Xie, Y., Vandermause, J., Sun, L., Cepellotti, A. & Kozinsky, B. Bayesian force fields from active learning for simulation of inter-dimensional transformation of stanene. *npj Comput. Mater.* **7**, 1–10 (2021).
- [35] Bhaumik, S. Synthesis and sintering of monolithic and composite ceramics under high pressures and high temperatures. *Metals Materials And Processes* **12**, 215–232 (2000).
- [36] Larsen, P. M., Schmidt, S. & Schiøtz, J. Robust structural identification via polyhedral template matching. *Modelling and Simulation in Materials Science and Engineering* **24**, 055007 (2016).
- [37] Stukowski, A. Visualization and analysis of atomistic simulation data with ovito—the open visualization tool. *Modelling and simulation in materials science and engineering* **18**, 015012 (2009).
- [38] Gayler, M. Melting point of high-purity silicon. *Nature* **142**, 478–478 (1938).
- [39] Zou, Y., Xiang, S. & Dai, C. Investigation on the efficiency and accuracy of methods for calculating melting temperature by molecular dynamics simulation. *Computational Materials Science* **171**, 109156 (2020).
- [40] Dozhdikov, V., Basharin, A. Y. & Levashov, P. Two-phase simulation of the crystalline silicon melting line at pressures from–1 to 3 gpa. *The Journal of Chemical Physics* **137**, 054502 (2012).

- [41] Dolloff, R. T. & Sara, R. *Research study to determine the phase equilibrium relations of selected metal carbides at high temperatures*, vol. 60 (Aeronautical Systems Division, Air Force Systems Command, US Air Force, 1961).
- [42] Daviau, K. & Lee, K. K. Zinc-blende to rocksalt transition in sic in a laser-heated diamond-anvil cell. *Physical Review B* **95**, 134108 (2017).
- [43] Kidokoro, Y., Umemoto, K., Hirose, K. & Ohishi, Y. Phase transition in sic from zinc-blende to rock-salt structure and implications for carbon-rich extrasolar planets. *American Mineralogist: Journal of Earth and Planetary Materials* **102**, 2230–2234 (2017).
- [44] Miozzi, F. *et al.* Equation of state of sic at extreme conditions: New insight into the interior of carbon-rich exoplanets. *J. Geophys. Res. Planets* **123**, 2295–2309 (2018).
- [45] Sekine, T. & Kobayashi, T. Shock compression of 6h polytype sic to 160 gpa. *Phys. Rev. B* **55**, 8034 (1997).
- [46] Tracy, S. *et al.* In situ observation of a phase transition in silicon carbide under shock compression using pulsed x-ray diffraction. *Phys. Rev. B* **99**, 214106 (2019).
- [47] Yoshida, M., Onodera, A., Ueno, M., Takemura, K. & Shimomura, O. Pressure-induced phase transition in sic. *Phys. Rev. B* **48**, 10587 (1993).
- [48] Kimoto, T. Bulk and epitaxial growth of silicon carbide. *Progress in Crystal Growth and Characterization of Materials* **62**, 329–351 (2016).
- [49] Zhou, J., Odqvist, J., Thuvander, M. & Hedström, P. Quantitative evaluation of spinodal decomposition in fe-cr by atom probe tomography and radial distribution function analysis. *Microscopy and Microanalysis* **19**, 665–675 (2013).
- [50] Sarkar, S. K., Ray, D., Sen, D. & Biswas, A. Nucleation–growth versus spinodal decomposition in fe–cr alloys: An experimental verification by atom probe tomography and small angle neutron scattering. *Microscopy and Microanalysis* **29**, 437–450 (2023).
- [51] Herrero, C. P., Ramírez, R. & Herrero-Saboya, G. Cubic silicon carbide under tensile pressure: Spinodal instability. *Chemical Physics* **573**, 112005 (2023). URL <https://www.sciencedirect.com/science/article/pii/S0301010423001878>.

- [52] Maras, E., Trushin, O., Stukowski, A., Ala-Nissila, T. & Jonsson, H. Global transition path search for dislocation formation in ge on si (001). *Computer Physics Communications* **205**, 13–21 (2016).

Supplementary Materials

Incongruent Melting and Phase Diagram of SiC from Machine Learning Molecular Dynamics

Yu Xie^{*,1}, Senja Ramakers^{2,3}, Menghang Wang¹, Frans Spaepen¹, and Boris Kozinsky^{†,1,4}

¹Harvard John A. Paulson School of Engineering and Applied Sciences

²Ruhr-Universität Bochum

³Robert Bosch GmbH

⁴Robert Bosch LLC

| | | |
|----------|--|----------|
| 1 | FLARE parameters | 2 |
| 2 | DFT parameters | 2 |
| 3 | Training data set | 2 |
| 4 | Figures | 4 |
| 4.1 | Radial distribution function | 4 |
| 4.2 | Snapshots of decomposition | 5 |
| 4.3 | Volume change during decomposition MD | 6 |
| 4.4 | High temperature transition from decomposed Si + C to homogeneous liquid | 7 |
| 4.5 | Low temperature transition from B1/B3 to decomposed Si + C | 8 |
| 4.6 | Snapshots of two-phase coexistence simulation | 9 |
| 4.7 | Influence of defect concentration | 10 |
| 4.8 | High-pressure zinc blende - rock salt transition | 11 |
| 4.9 | Gas phase volume change | 12 |
| 4.10 | Spatial correlation function | 13 |
| 4.11 | Uncertainty monitoring | 14 |

*yuxie1@microsoft.com.

†bkoz@seas.harvard.edu

1 FLARE parameters

| FLARE | Parameter | Value |
|-------------------------------|---|-------------------------------|
| Descriptor | ACE Descriptor | B2 |
| | n_{max} | 8 |
| | l_{max} | 3 |
| | Cutoff | 4.0 (Å) |
| Kernel and GP hyperparameters | Kernel | Normalized dot product |
| | Power (ξ) | 2 |
| | Signal variance σ | 13.8670 |
| | Energy noise σ_e | 0.6039 (eV) |
| | Force noise σ_f | 0.4240 (eV/Å) |
| | Stress noise σ_s | 0.0063 (eV/Å ³) |
| | Single atom energies | C: -9.1009 eV, Si: -5.4250 eV |
| Active learning | Threshold of calling DFT | 0.03 |
| | Threshold of adding sparse environments | 0.006 |

Table 1: Parameters for descriptors, kernels, Gaussian process and active learning in FLARE.

2 DFT parameters

| Parameter | Value |
|---------------------------------|-------------------------|
| Exchange-correlation functional | PBE |
| Energy cutoff (ENCUT) | 800 eV |
| Smearing (ISMear) | Gaussian (0) |
| Smearing width (SIGMA) | 0.03 eV |
| Convergence condition (EDIFF) | 1.0e-5 eV for 64 atoms |
| | 1.0e-4 eV for 512 atoms |
| K-point | 3x3x3 for 64 atoms |
| | 1x1x1 for 512 atoms |

Table 2: DFT parameters used in VASP.

3 Training data set

The active learning workflow collected 2088 DFT frames. The offline training from all the DFT data selected 471 frames to add to the final model.

| Data | Temperature (K) | Pressure (GPa) | # DFT frames |
|-----------------------------------|------------------------|-----------------------|---------------------|
| ZB \leftrightarrow RS data [?] | 300 - 2000 | 0 - 500 | 680 |
| Si (start from cubic diamond) | 1000 - 3000 | 0 - 120 | 46 |
| C (start from cubic diamond) | 2000 - 4000 | 0 - 120 | 55 |
| C (start from graphite) | 2000 | 0 - 120 | 30 |
| SiC (64 atoms) | 2000 - 6000 | 0 - 120 | 1128 |
| SiC (512 atoms) | 5000 | 0 - 120 | 149 |

Table 3: Training data set. The ZB \leftrightarrow RS data comes from our previous publication [?].

4 Figures

4.1 Radial distribution function

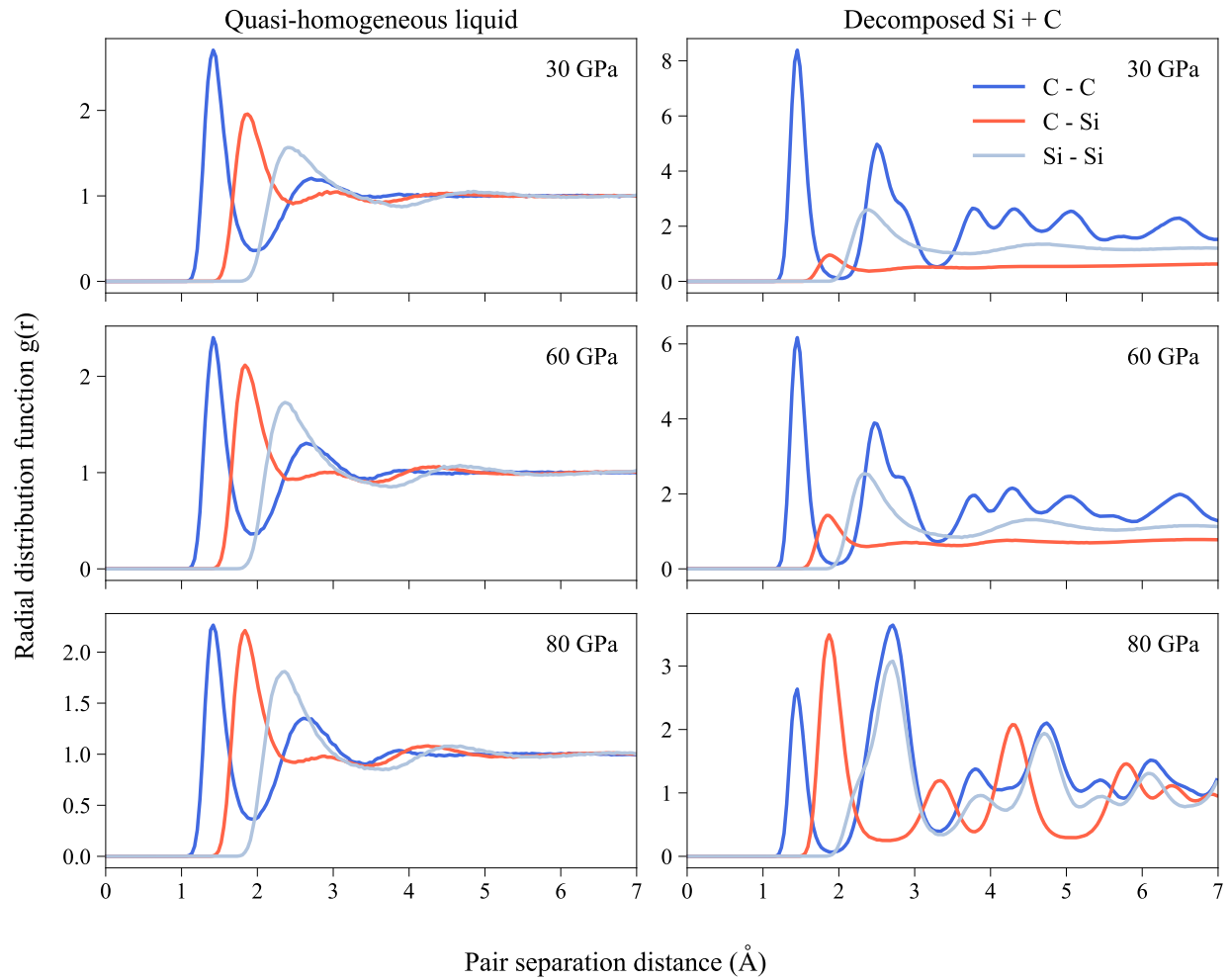


Figure 1: Radial distribution function of the high-temperature amorphous SiC.

4.2 Snapshots of decomposition

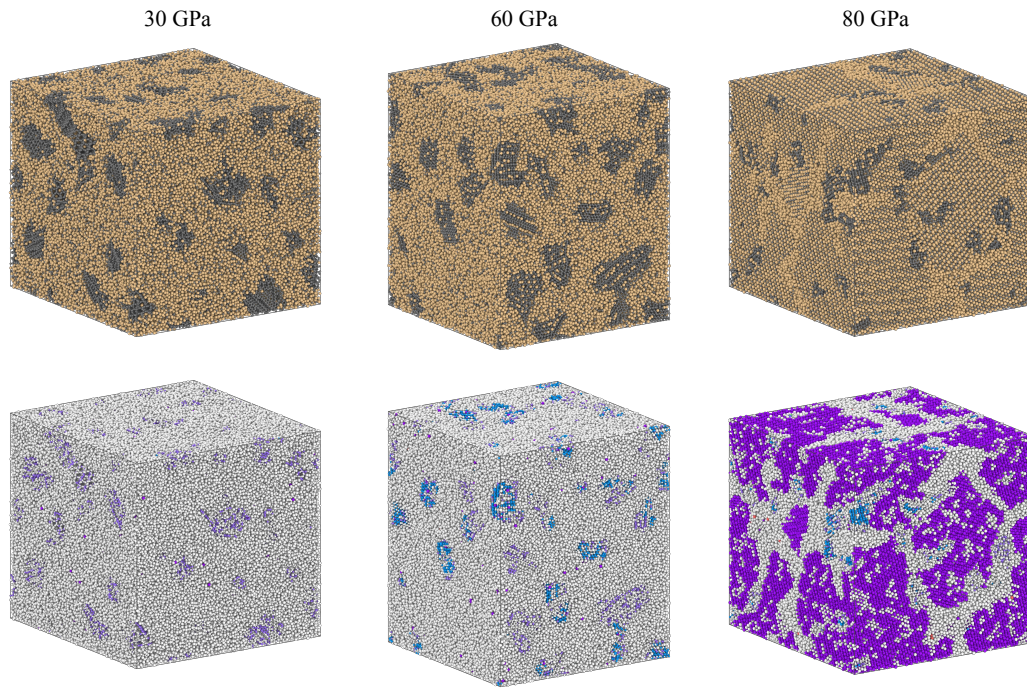


Figure 2: 0.5M atoms configuration at 30 GPa, 60 GPa and 80 GPa. Top row: the decomposed configuration at the end of cooling process at 3000 K with atoms colored by chemical elements (Orange: Si, black: C). Bottom row: the same configuration as the top row, but colored by crystal types classified with polyhedral template matching (Blue: cubic diamond, light purple: graphene, dark purple: simple cubic).

4.3 Volume change during decomposition MD

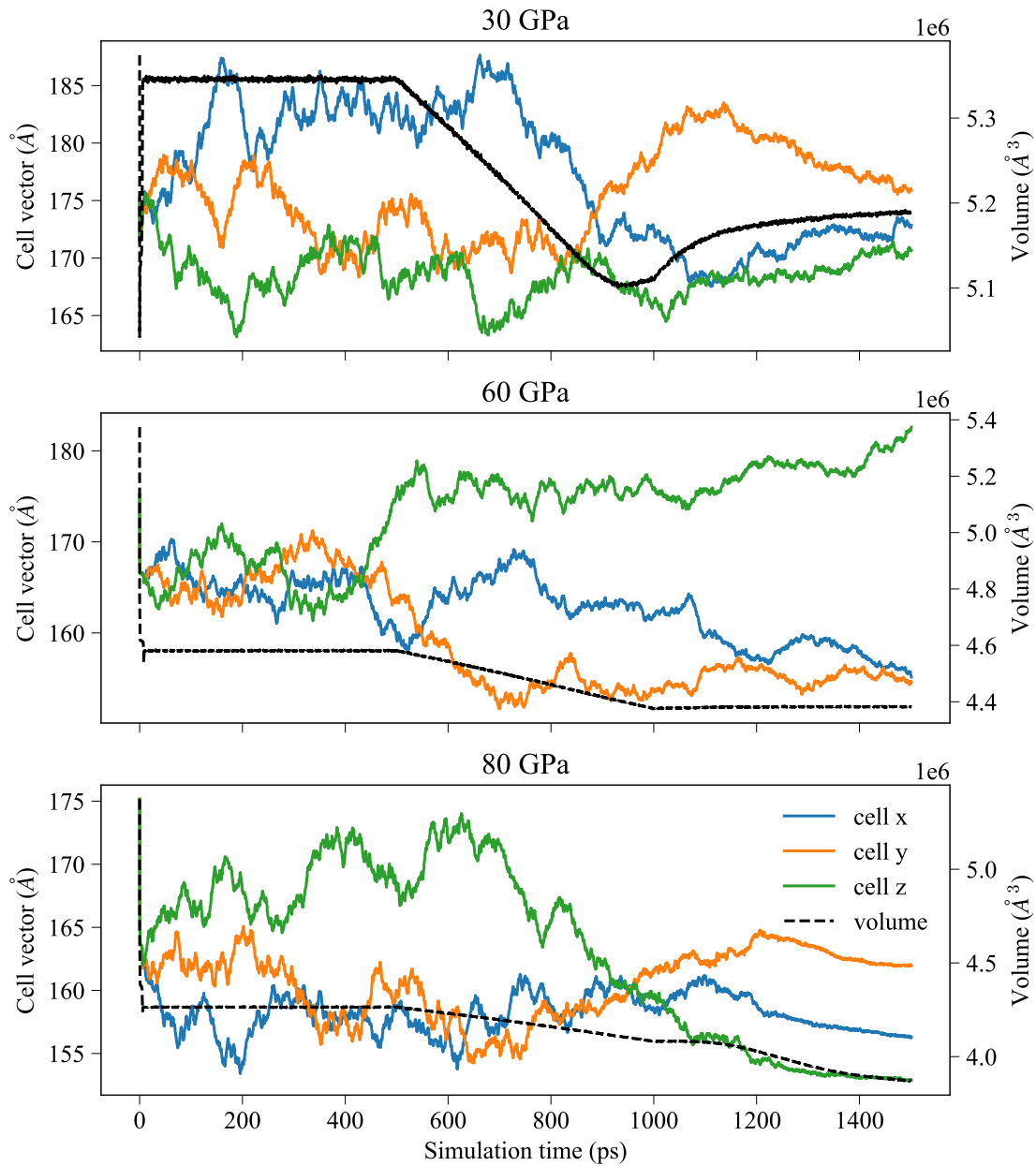


Figure 3: 0.5M atoms cell dimension and volume at 30 GPa, 60 GPa and 80 GPa.

4.4 High temperature transition from decomposed Si + C to homogeneous liquid

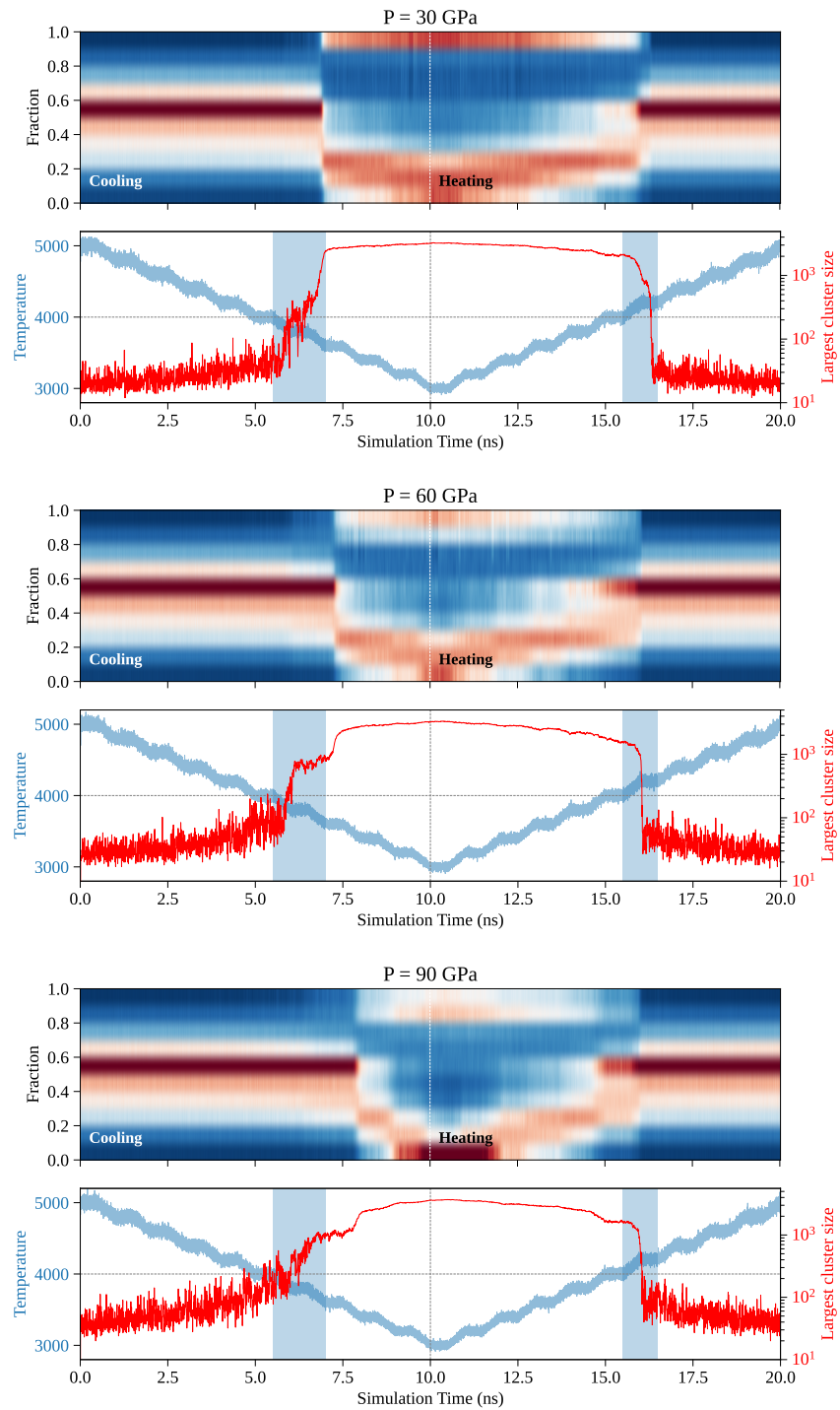


Figure 4: Cooling and heating of SiC for the transition between Si + C and near homogeneous liquid at 60 and 90 GPa.

4.5 Low temperature transition from B1/B3 to decomposed Si + C

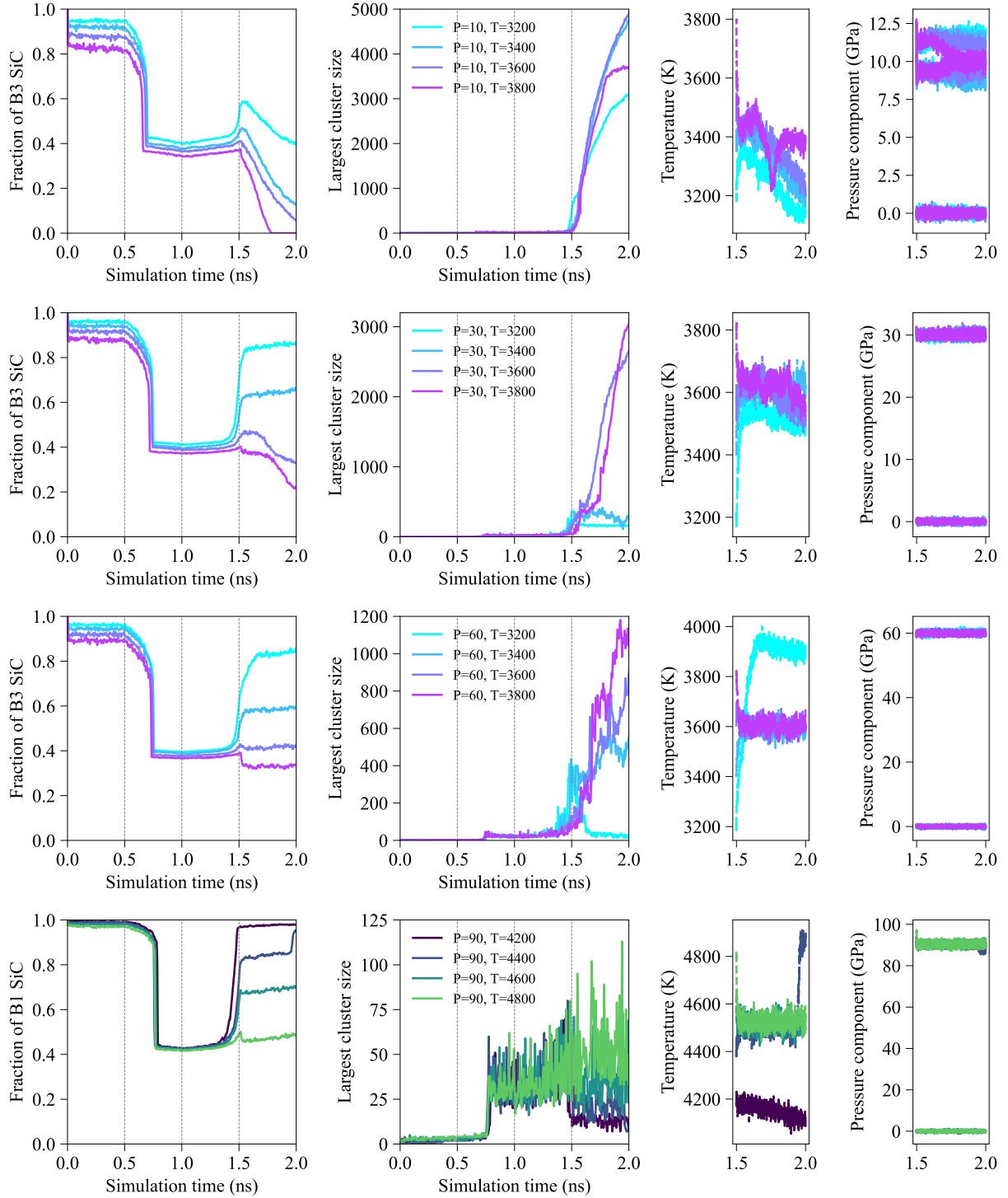
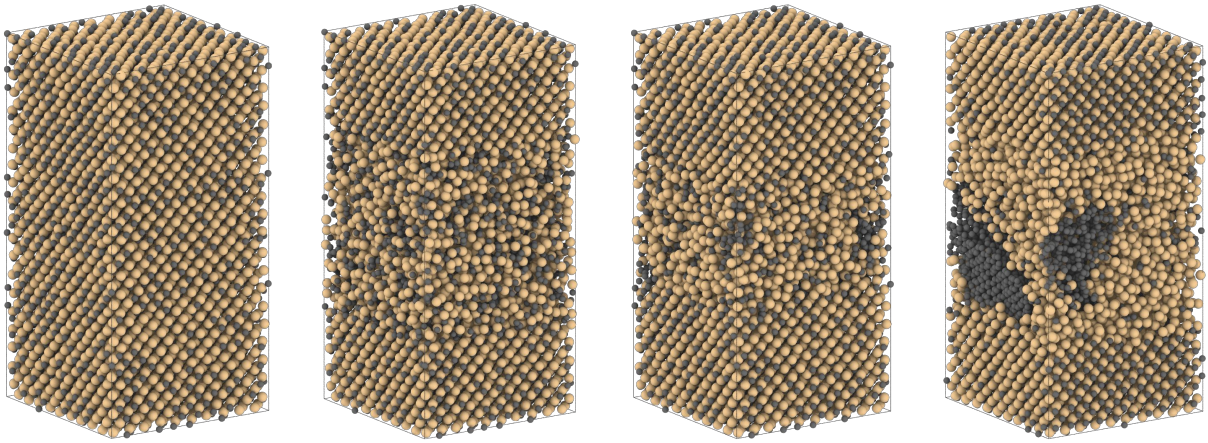


Figure 5: Two-phase MD cluster and structural analysis for 10, 30, 60 and 90 GPa.

4.6 Snapshots of two-phase coexistence simulation

P = 10 GPa



P = 60 GPa

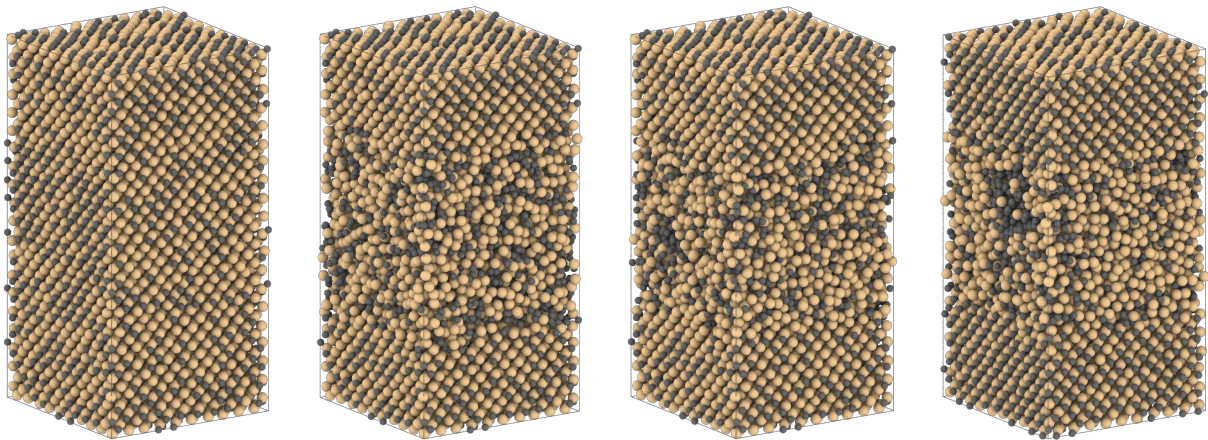


Figure 6: Two-phase MD snapshots at pressures 10, 30 and 60 GPa, starting at B3 phase (zinc blende, cubic diamond lattice).

4.7 Influence of defect concentration

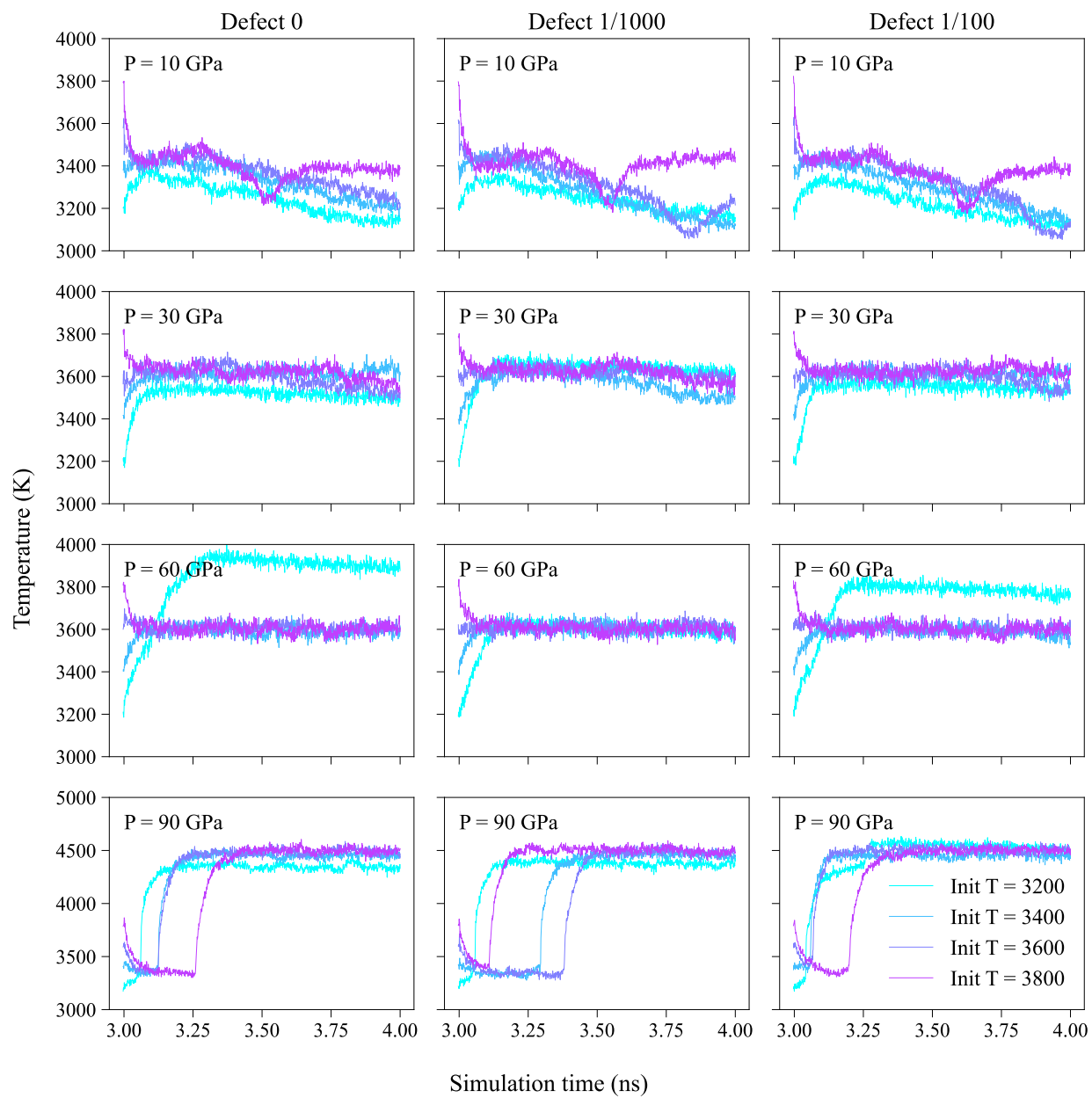


Figure 7: Two-phase results with different defect concentrations.

4.8 High-pressure zinc blende - rock salt transition

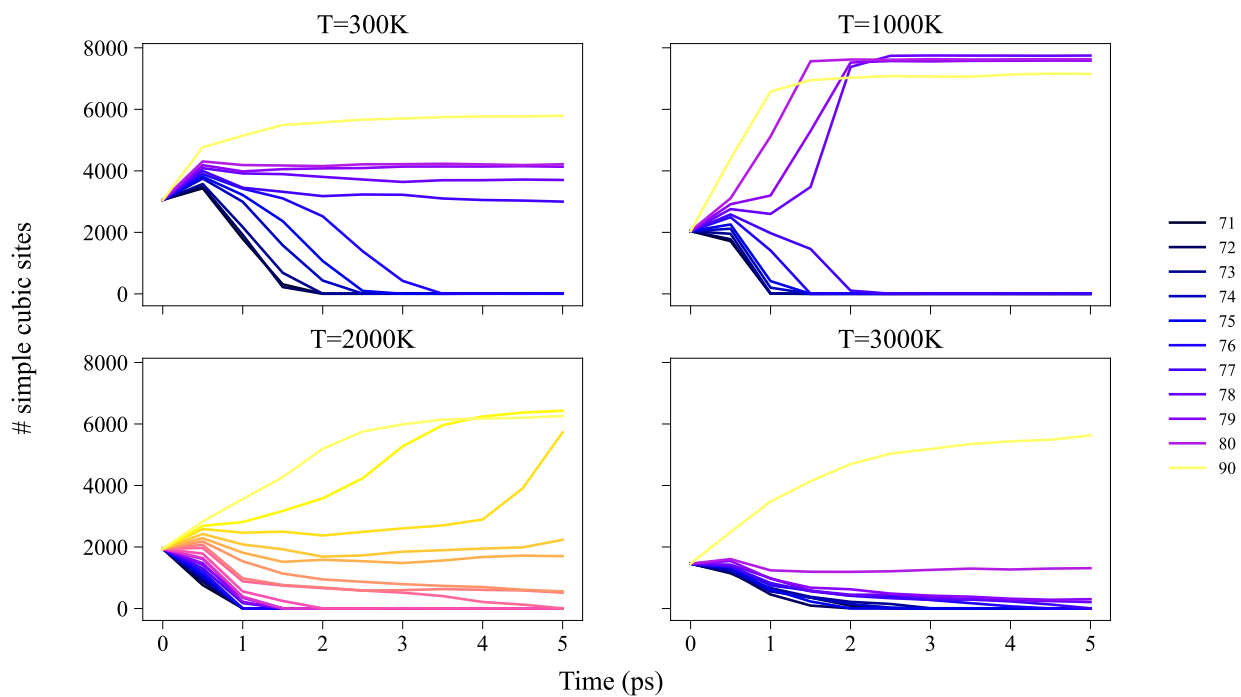


Figure 8: B3→B1 pressure scan plots (pressure unit: GPa).

4.9 Gas phase volume change

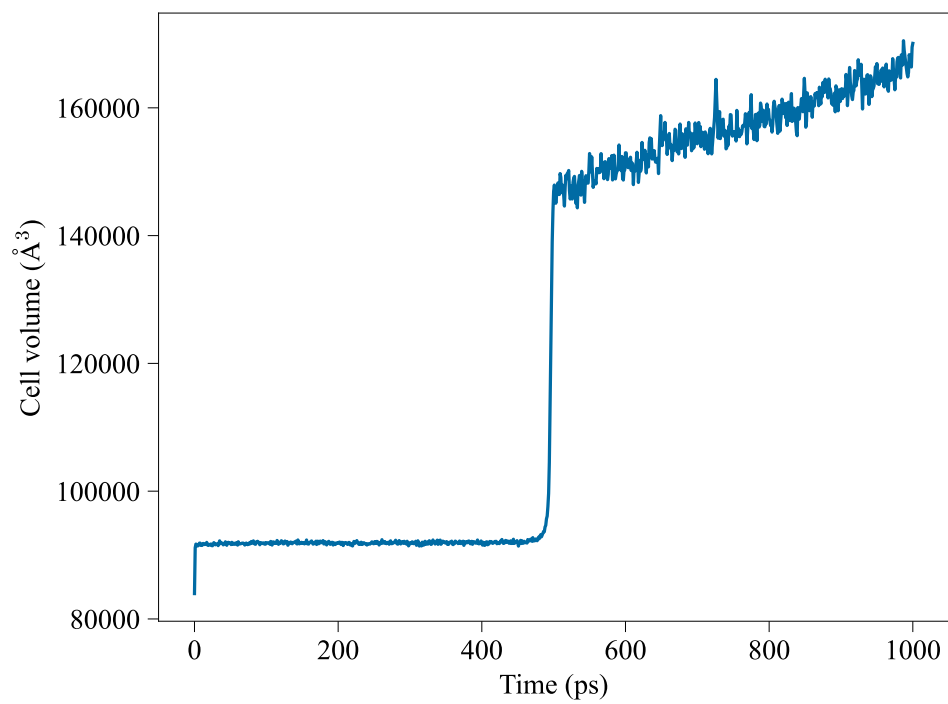


Figure 9: $T = 4000$ K, low pressure, the volume keeps going up.

4.10 Spatial correlation function

To investigate the spatial distribution of concentration of the decomposed structure, one approach is to compute the radial distribution function. However, the characteristic size of the clusters is a few nanometers. When looking at individual particles, the calculation of radial distribution function with cutoff beyond 2 nm can be very slow.

Therefore, we instead look at the continuous model with local concentration. Basically, we discretize the super cell into small bins and compute the local carbon concentration which is the number of carbon atoms in the bin divided by the volume of the bin. Then we compute the spatial correlation function w.r.t. distance $g_{AB}(r) = \langle c_A(0)c_B(r) \rangle$ with A and B representing chemical elements and $c(r)$ is the concentration at distance r .

In the C-C correlation function $g_{CC}(r)$ as shown in the figure below, we observe the peak at around 4 nm corresponding to the statistically averaged distance between two C-rich regions. It also indicates the wavelength of the spinodal decomposition mode of SiC phase separation [? ?].

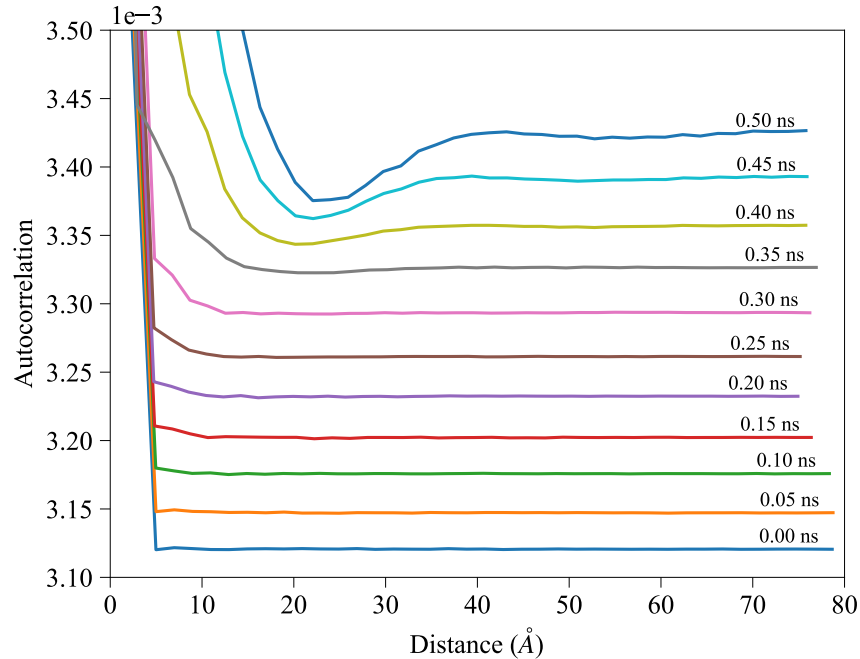


Figure 10: Spatial correlation function of C-C. P=60 GPa, cooling down from 5000K (0 ns) to 3000K (0.5 ns).

4.11 Uncertainty monitoring

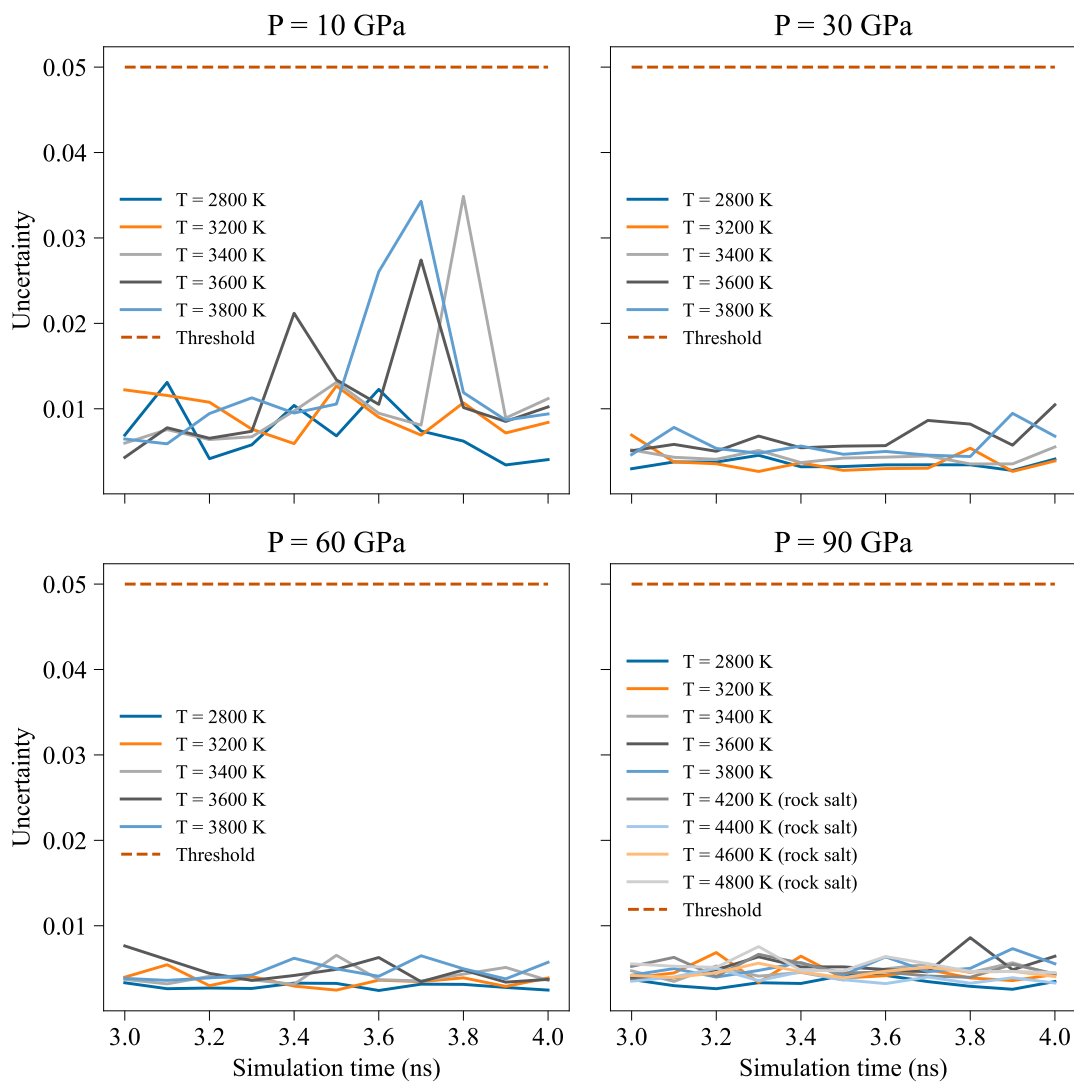


Figure 11: Uncertainty validation of the two-phase MD simulation.